## A Chandra X-ray study of the mixed-morphology supernova remnant 3C 400.2

Broersen, S.; Vink, J.

[Link to publication](Link to publication)

# A *Chandra* X-ray study of the mixed-morphology supernova remnant 3C 400.2

## Sjors Broersen[1] and Jacco Vink[1,2]★

[1]*Astronomical Institute 'Anton Pannekoek', University of Amsterdam, Postbus 94249, NL-1090 GE Amsterdam, the Netherlands*
[2] *GRAPPA, University of Amsterdam, Postbus 94249, NL-1090 GE Amsterdam, the Netherlands*

## ABSTRACT

We present an analysis of archival *Chandra* observations of the mixed-morphology remnant 3C 400.2. We analysed spectra of different parts of the remnant to observe if the plasma properties provide hints on the origin of the mixed-morphology class. These remnants often show overi-ionization, which is a sign of rapid cooling of the thermal plasma, and supersolar abundances of elements which is a sign of ejecta emission. Our analysis shows that the thermal emission of 3C 400.2 can be well explained by a two-component non-equilibrium ionization model, of which one component is underionized, has a high temperature ($kT \approx 3.9$ keV) and supersolar abundances, while the other component has a much lower temperature ($kT \approx 0.14$ keV), solar abundances and shows signs of overionization. The temperature structure, abundance values and density contrast between the different model components suggest that the hot component comes from ejecta plasma, while the cooler component has an interstellar matter origin. This provides the first evidence of an overionized plasma found in the outer regions of a supernova remnant, whereas the ejecta component of the inner region is underionized. In addition, the non-equilibrium ionization plasma component associated with the ejecta is confined to the central, brighter parts of the remnant, whereas the cooler component is present mostly in the outer regions. Therefore, our data can most naturally be explained by an evolutionary scenario in which the outer parts of the remnant are cooling rapidly due to having swept-up high-density ambient medium, while the inner parts are very hot and cooling inefficiently due to low density of the plasma. This is also known as the relic X-ray scenario.

**Key words:** supernovae: general – supernovae: individual: 3C 400.2 – ISM: supernova remnants.

## 1 INTRODUCTION

An important and not well-understood class of supernova remnants (SNRs) are the so-called thermal composite or mixed-morphology remnants (MMRs; Rho & Petre 1998; Lazendic & Slane 2006; Vink 2012). These remnants are characterized by thermal X-ray emission that is centrally peaked whereas the radio emission has the familiar shell-type morphology. They have several other interesting characteristics: they are often associated with GeV gamma-ray emission (e.g. Giuliani et al. 2010; Uchiyama et al. 2012), there is evidence for enhanced metal abundances in some of them (Lazendic & Slane 2006) although they are usually mature remnants, and they often show spectral features associated with strong cooling in the form of radiative recombination continua (RRCs) or strong He$\alpha$/Ly$\alpha$ X-ray line ratios of alpha-elements such as Si, S and Ar (Kawasaki et al. 2005).

The centrally peaked X-ray emission of MMRs poses a problem for SNR evolution models. They typically have an age of the order of 20 000 yr and are therefore expected to have a shell-like density structure with a hot, tenuous plasma in the centre, based on a Sedov evolutionary scenario. A flat interstellar matter (ISM) structure is therefore unsuited to create the centre-filled X-ray morphology that is observed, if the temperature is relatively uniform across the remnant. Rho & Petre (1998) mention two possible scenarios for the formation of the emission structure typical for MMRs, the *relic X-ray emission* and the *evaporating cloudlet* scenario (White & Long 1991). The former scenario is the most simple scenario, in which the outer layers of the remnant have become radiative and have cooled strongly so that they hardly emit in the X-ray band, whilst the centre consists of hot plasma that has not yet cooled below $10^6$ K. This scenario requires a high surrounding ambient medium density. White & Long (1991) give a self-similar solution for a supernova that exploded in an environment where it is surrounded by a number of small, dense clouds. Due to the large filling fraction and small size of the clouds they do not alter the dynamics of the

★ E-mail: j.vink@uva.nl

forward shock, and they survive the passage of the forward shock due to their large density. The clouds then slowly evaporate due to heating by thermal conduction, which increases the density and decreases the temperature in the centre of the remnant. Of these two scenarios, the relic X-ray emission scenario was preferred by Harrus et al. (1997) to explain the morphology of W44. One year later, Cox et al. (1999) and Shelton et al. (1999) used a similar scenario as Harrus et al. (1997) to model the characteristics of the MMR W44, but added a density gradient for the ISM and thermal conduction. Thermal conduction in the model by Cox et al. (1999) smoothes the temperature gradient from the centre to the outer layers, thereby reducing the pressure in the centre. A lower central pressure reduces the need to expand, which allows for a higher density to remain in the centre of the remnant. A problem with the scenarios using thermal conduction is that it is not a priori clear whether it can be important in SNRs, since it is strongly suppressed by magnetic fields (Spitzer 1981; Tao 1995).

Clear evidence for overionization of thermal SNR plasmas is almost exclusively found in MMRs. Thermal plasmas in SNRs are often found in an underionized state, and reach ionization equilibrium on a density-dependent time-scale $t \simeq 10^{12.5}/n_e$ s (Smith & Hughes 2010). Due to their ages and their frequent association with high-density regions, MMRs are expected to have a plasma that is in ionization equilibrium. The fact that there is ample evidence for overionization, means the cooling rate of the plasma was faster than the recombination rate. How the rapid cooling proceeds is still unclear. Efforts have been made to localize regions in MMRs which are cooling rapidly, as an association with a high-density region may mean that thermal conduction is important. For example: Miceli et al. (2010) and Lopez et al. (2013) find that the amount of cooling increases away from a molecular cloud for W49B, suggesting adiabatic cooling as the dominant cooling mechanism. Uchida et al. (2012) suggest the cooling time-scale of the plasma cannot be explained by thermal conduction, and that adiabatic expansion is probably the dominant cause for cooling there. In addition, Broersen et al. (2011) have shown that even at small expansion rates, simple adiabatic cooling combined with cooling through X-ray radiation can lead to a cooling rate of the plasma larger than the recombination rate. So far observational evidence for strong thermal conduction is lacking.

The ionization state of a thermal plasma can be determined by using both the electron temperature $T_e$ and the so-called ionization temperature $T_z$ (Masai 1997). The ionization temperature is the electron temperature that one would deduce from the ionization state of X-ray emitting elements alone, which may be different from the thermodynamic temperature in case the plasma is not in ionization equilibrium. When $T_z < T_e$, the plasma is underionized, when $T_z = T_e$ the plasma is in collisional ionization equilibrium (CIE) and when $T_z > T_e$ the plasma is overionized. There are different ways in which $T_z$ can be determined. Kawasaki et al. (2002) determine $T_z$ by comparing the observed Ly$\alpha$/He$\alpha$ ratio of a certain element to the ratios of CIE plasmas of different temperatures. The temperature of the CIE plasma that produces the observed ratio is then $T_z$. A different method was used by Ohnishi et al. (2011), who determined $T_z$ by using the CIE model in SPEX to fit the plasma. This model has an additional parameter $\xi$, compared to the XSPEC CIE model. This parameter can be used to simulate a non-equilibrium plasma so that $T_z = \xi \times T_e$. Finally, there is the method used by Broersen et al. (2011) and Uchida et al. (2012), who fit a plasma using the SPEX non-equilibrium ionization (NEI) model with initial temperature $kT_1 > kT_2$. $kT_1$ has a similar function as the ionization temperature, but it has a slightly different physical meaning as it
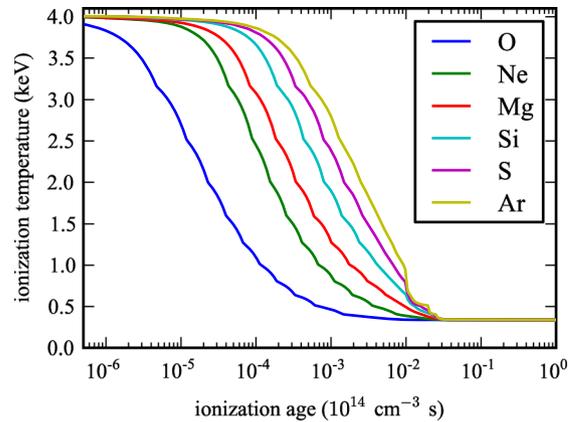


**Figure 1.** The ionization temperature of a plasma versus the ionization age. The NEI plasma starts at an electron and ionization temperature of 4.0 keV, and it evolves after the electron temperature instantly drops to 0.2 keV. The figure illustrates that the NEI and line-ratio/ionization-temperature methods for characterizing overionized plasma do not provide identical ionization states. Moreover, the differences depend on the element: at certain ionization ages, different elements may have different ionization temperatures.

describes the initial ionization state. The NEI model then follows the ionization state as a function of ionization age ($n_e t$), assuming a rather sudden drop of electron temperature. Note that although using the He$\alpha$/Ly$\alpha$ line ratios of alpha elements can show that a plasma is overionized, it has quite a large systematic error in determining the $T_z$ (Lopez et al. 2013). This is the result of the fact that there are emission lines of other elements which contaminate the He$\alpha$ /Ly$\alpha$ ratio. The strengths of the contaminating lines are $T_e$ dependent, so that the systematic error is $T_e$ dependent as well. This can be taken into account by calculating the CIE line ratios including the contaminating lines.

The difference in ionization temperature between the line ratio and NEI model methods is displayed in Fig. 1. This figure shows the evolution of the ionization temperature as a function of ionization age, for an NEI plasma that is cooling abruptly from 4 to 0.2 keV. It is clear from the figure that different elements show different ionization temperatures as the plasma evolves, so that a plasma cannot be characterized by a single ionization temperature. More specifically, elements with a higher charge (high $Z$) are out of ionization equilibrium for a longer time. This also explains why different elements in SNR plasmas often show different ionization temperatures, as found by e.g. Lopez et al. (2013). On the other hand the NEI model is not a perfect model for a cooling plasma, as it assumes the electron temperature instantly drops to a certain value. In reality the electron temperature will drop more gradual, so that the plasma evolution will be slightly different as a result of different recombination and ionization rates.

Here, we present the first analysis of a *Chandra* X-ray observation of 3C 400.2 (also known as G53.6 − 2.2), which is an important member of the MMR class. This remnant has centrally peaked X-ray emission, as shown by *Einstein* Image Proportional Counter and *ROSAT* observations (Long et al. 1991; Saken et al. 1995). The radio morphology can be described as two overlapping circular shells of diameters 14 and 22 arcmin (Dubner et al. 1994). This has led to the speculation that 3C 400.2 might be two SNRs in contact with each other, which would make it a rare event. Yoshita et al. (2001) conclude however, using *ASCA* observations, that the remnant is the result of a single supernova explosion, based on the similar plasma properties found in the two shells. Hydrodynamical

simulations, including thermal conduction, show that the morphology of the remnant can be explained by a supernova exploding in a cavity, where the larger shell is a part of the remnant expanding into a lower density region than the smaller shell (Schneiter, de La Fuente & Velázquez 2006). This is consistent with H I observations performed by Giacani et al. (1998), who find a denser region to the north-west of the remnant where the smaller shell is located. In the optical, the remnant is characterized by a shell-like structure with a smaller radius (about 8 arcmin) than the radio shell (Winkler, Olinger & Westerbeke 1993; Ambrocio-Cruz, Rosado & de La Fuente 2006). The optical emission is located in regions of low X-ray emissivity. Optical emission suggests that those parts of the remnant contain radiative shocks, and are therefore cooling efficiently. Distance estimates to 3C 400.2 range from 2.3–6.9 kpc (Milne 1979; Rosado 1983; Dubner et al. 1994; Giacani et al. 1998). However, the distance estimates based on radio data are obtained with the uncertain $\Sigma$–$D$ relationship, and the kinematic estimate of Rosado (1983) is based on interferograms of a small part of the remnant. We therefore consider the most recent distance estimate of $2.3 \pm 0.8$ kpc (Giacani et al. 1998), which is based on H I measurements, as the more reliable one and we will use a round value of 2.5 kpc for the distance throughout this paper.

MMRs and in particular overionization of plasmas have gathered increasing attention over the past few years. In this work, we therefore aim to characterize the plasma properties of 3C 400.2 in order to increase our understanding both of overionized plasmas, and the possible evolutionary scenarios of MMRs. We start with the data reduction and spectral analysis of different regions of the remnant, which is followed by a discussion on the measured plasma properties. We end with the conclusions.

## 2 DATA ANALYSIS AND RESULTS

### 2.1 Data reduction

In this paper, we report on the analysis of a 34 ks archival *Chandra* observation (ObsID 2807) taken on 2002 August 11 with *Chandra* observing in imaging mode with the Advanced CCD Imaging Spectrometer (ACIS)-I CCD array. The total number of counts in the 0.3–7.0 keV band in the full spectrum is ~58 k. We extracted spectra using the default tasks in the *Chandra* analysis software CIAO version 4.5, using the task *specextract* to create spectra and weighted responses (RMF and ARF). We removed point sources from the spectral extraction regions. The spectra where grouped so that each bin contained a minimum of 15 counts. The remnant covers the whole area of the ACIS-I chips (see Fig. 2), and there was no region available for background extraction. We therefore used the standard ACIS-I background files to create background spectra. We used SPEX version 2.03 (Kaastra, Mewe & Nieuwenhuijzen 1996) for the spectral modelling. The NEI model in SPEX is an extended version of the MEKAL code used in XSPEC (Arnaud 1996), with the added advantage that the initial temperature of the NEI model can be varied to mimic an overionized plasma.

### 2.2 Spectral analysis

The *Chandra* ACIS-I field of view (FOV) covers the part of the remnant that is mostly associated with the smaller radio shell. It includes the brightest part of the remnant in X-rays, as can be deduced from the *ROSAT* image in Fig. 2. With our spectral analysis, we aim to find differences in plasma properties between different parts of the remnant, and to investigate if this remnant conforms
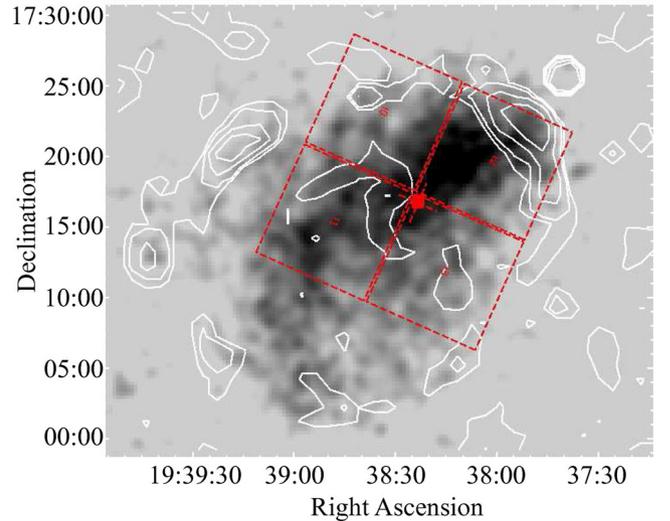


**Figure 2.** *ROSAT* Position Sensitive Proportional Counters image in an inverted grey-scale, with NRAO VLA Sky Survey (NVSS, Condon et al. 1998) contours overlaid. The *Chandra* ACIS-I FOV is indicated in red.

to the general properties of MMRs mentioned in the introduction, with regards to overionization and abundances.

We fitted the spectra using absorbed NEI models, of which the parameters are the ionization age $\tau = n_e t$, the electron temperature $kT_2$, the elemental abundances and the normalization $n_e n_H V$. A CIE plasma is identical to an NEI plasma when $\tau \geq 10^{12.5}$ cm$^{-3}$ s. In addition to the above listed parameters, the SPEX NEI model has the initial temperature of the plasma, $kT_1$, as an optional parameter. As mentioned in the Introduction, putting $kT_1 > kT_2$ makes the NEI model mimic an overionized plasma, where the ionization state of the plasma is determined by $kT_1$ and $\tau$, while the continuum shape is determined by the electron temperature $kT_2 = kT_e$. The method to check for overionization using Ly$\alpha$ and He$\alpha$ line strengths is not feasible for 3C 400.2, since elements with isolated emission lines such as Si and S show no significant Ly$\alpha$ lines in this remnant.

We aimed to first find a satisfactory fit for the region covering almost the full area of the ACIS-I chips (see Fig. 4), where we initially tried to fit the spectrum with an absorbed, single, underionized NEI model with fixed abundances, freeing abundances only when it led to a significant improvement in C-stat/degrees of freedom (d.o.f.) (Cash 1979). The $N_H$ was always allowed to vary. A single absorbed NEI model was not sufficient to obtain an acceptable C-stat/d.o.f. in any of the extracted spectra, however.

The next step was to try to fit the spectrum with a double NEI model. Although the C-stat/d.o.f. improved significantly with respect to a fit with a single NEI model, the fit was still not acceptable. The only way the fit of the double NEI models became acceptable, was by allowing the $kT_1$ of the cooler NEI component to vary, so that $kT_1 > kT_2$, and therefore the NEI plasma is overionized. We show in detail why the overionized model fits the data better than an underionized model in Section 2.2.1.

Fig. 3 shows the spectrum of the full region and the spectral extraction regions are shown in Fig. 4. The best-fitting model for this region consists of a $kT = 3.86$ keV plasma with supersolar abundances plotted as a green dashed line, combined with a $kT_2 = 0.14$ keV, overionized NEI component which is plotted as a blue dot–dashed line. The parameters of the model are listed in Table 1. It is clear from the figure that the high-$kT$ model accounts for the bulk of the Fe-L (0.7–1.2 keV), Si XIII (1.85 keV) and S XV
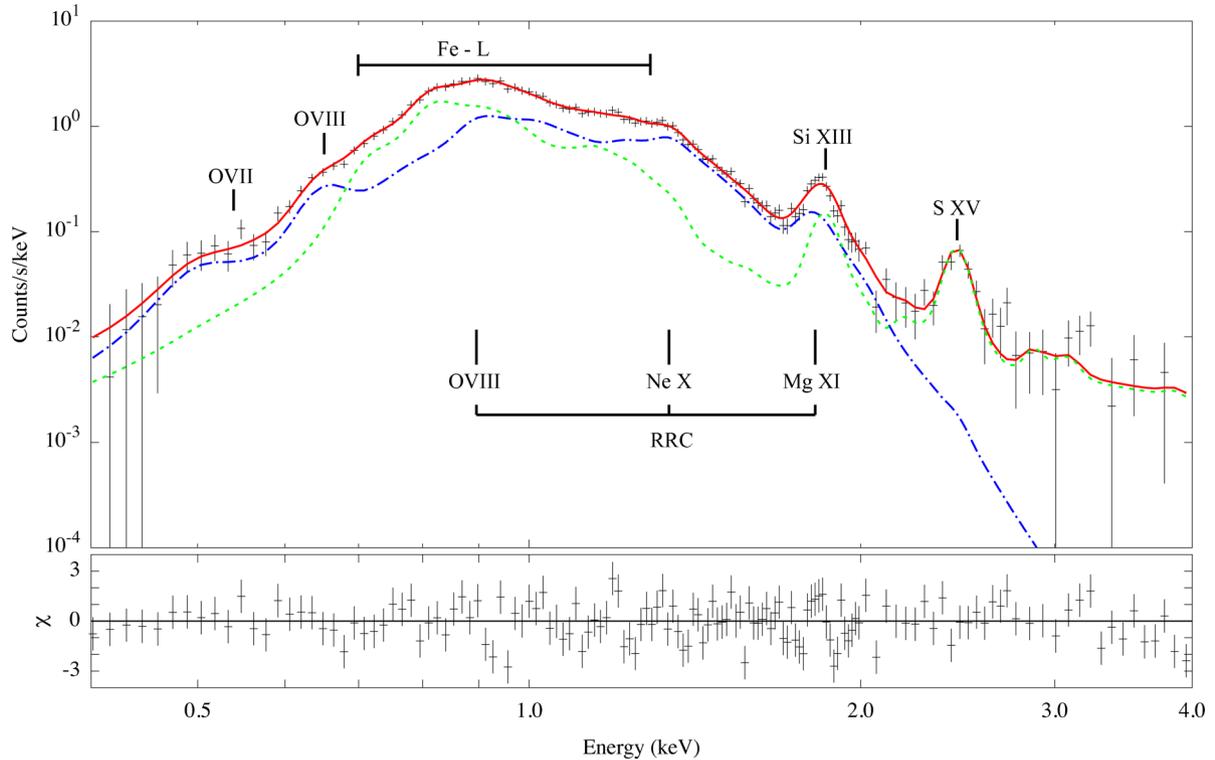
**Figure 3.** Spectrum of the region covering almost the whole area of the ACIS-I chips. The blue dash–dotted line shows the low-*kT* overionized NEI component, while the green dashed line shows the high-*kT* underionized NEI component. The parameters of the model are listed in Table 1. Indicated in the figure are the locations of the O VIII, Ne X and Mg XI RRCs which are present in the overionized model (blue dash–dotted line) and the locations of important emission lines. The green dashed line represents the hot NEI component.
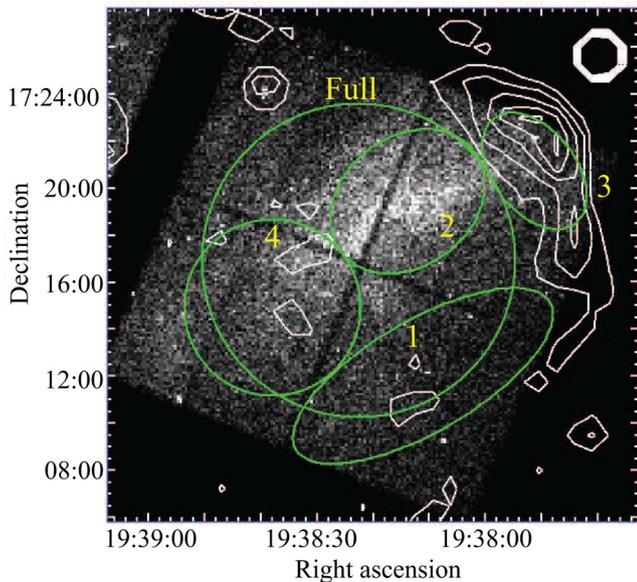


**Figure 4.** *Chandra* image in the 0.3–7.0 keV band with NVSS radio contours. The extraction regions of the spectra are labelled in yellow.

**Table 1.** The best-fitting model parameters of the spectrum covering the whole area of the ACIS-I chips. We used the solar abundances from Anders & Grevesse (1989). Note that the hot ejecta plasma is underionized, while the ISM component is overionized. The errors represent the $1\sigma$ confidence interval.

| Component | Parameter | Unit | Value |
|---|---|---|---|
| Ejecta | $N_H$ | $10^{21}$ cm$^{-2}$ | $6.08^{+0.15}_{-0.12}$ |
| | $n_e n_H V$ | $10^{55}$ cm$^{-3}$ | $2.31^{+0.83}_{-0.67}$ |
| | $kT_e$ | | $3.86^{+0.30}_{-0.28}$ |
| | $\tau$ | $10^{10}$ cm$^{-3}$ | $2.02^{+0.05}_{-0.06}$ |
| | Si | | $3.11^{+1.23}_{-0.84}$ |
| | S | | $6.09^{+2.73}_{-1.80}$ |
| | Fe | | $16.6^{+7.2}_{-4.8}$ |
| | Luminosity | $10^{31}$ erg s$^{-1}$ | 68 |
| ISM | $n_e n_H V$ | $10^{58}$ cm$^{-3}$ | $1.17^{+0.21}_{-15}$ |
| | $kT_1$ | | $0.42^{+0.03}_{-0.02}$ |
| | $kT_e$ | | $0.14^{+0.01}_{-0.01}$ |
| | $\tau$ | $10^{10}$ cm$^{-3}$ s | $26.4^{+7.8}_{-6.03}$ |
| | Ne | | $0.40^{+0.04}_{-0.04}$ |
| | Luminosity | $10^{31}$ erg s$^{-1}$ | 4.5 |
| | C-stat/d.o.f. | | 257.84/228 |

(2.46 keV) line emission, while the low-*kT* model accounts for the O VII–VIII (0.56 and 0.65 keV) line emission, and continuum emission in the form of O VIII, Ne X and Mg XI RRCs. The supersolar abundances of Si, S and Fe in the hot NEI component suggest an ejecta origin for the plasma. The abundances of the high-*kT* component as well as the emission measure have quite large errors. This is caused by the fact that the continuum shape at energies larger than

2.5 keV is not well defined by the data. The reason is that for higher photon energies the statistical error is larger due to lower count rates and a relatively higher background. Uncertainties in the continuum strength cause large formal errors in the abundances, since

the strength of the continuum and the height of the abundances are anticorrelated. None the less, the abundances are significantly super solar, which means that 3C 400.2 belongs to the group of MMRs with supersolar abundances. Overionization is found only in the lower *kT* plasma, and not in the high-*kT* plasma. Making the initial temperature a free parameter in the hot NEI component did not improve the fit. There is therefore no evidence for overionization in the ejecta component, which is further corroborated by the absence of strong Lyα lines of Si and S. The abundances of the low-*kT* NEI component are sub-solar in the case of NE and O and solar for all other elements, which suggest a swept-up ISM origin for this plasma.

Overall the fit is acceptable at a C-stat/d.o.f. of 257/227, although there are some significant residuals. The most notable residual feature is found at the position of the Si XIII–XIV line at 1.85 keV. The model fits this line partly with the Mg XI RRC from the cool NEI component, and partly with Si emission from the hot component. It seems that the ionization state of Si in the hot component is somewhat too high. This may be caused by the fact that this spectrum was taken from a large region of the remnant, in which in different parts the Si may be in different ionization states. The parameters obtained from this spectral fit will be used in the discussion to determine the overall physical parameters of the remnant.

Our best-fitting model differs significantly from results obtained previously. The most recent X-ray observations of 3C 400.2 were performed by Yoshita et al. (2001), using the Gas Imaging Spectrometer instrument onboard *ASCA* X-ray telescope. The $N_\mathrm{H}$ that we find is quite similar to theirs, but they find an acceptable fit for this region using a single NEI model with $kT = 0.8$ keV and $\log(\tau) = 10.7$–$11.2$ cm$^{-3}$ s. We have tried to fit our data with a single NEI model like this, but this gives a C-stat/d.o.f. = 606.23/229, even when allowing multiple abundances to vary. The differences in best-fitting parameters most likely stem from the fact that the *Chandra* ACIS instrument has a higher spectral resolution than the GIS instrument, allowing for better constraints on plasma parameters.

### 2.2.1 Overionization

Although overionization is a common feature of MMRs, it is not immediately clear that the plasma is overionized in 3C 400.2, due to the lack of strong, isolated RRC features. Overionization in this remnant has a more subtle presence, which we illustrate in Fig. 5. This figure shows a close-up of the full spectrum shown in Fig. 3 in the energy range 0.5–1.7 keV, where the red line represents the best-fitting model without overionization, and the dashed blue line the best-fitting overionized model. The bottom panel of the figure shows the residuals of the non-overionized model, with plotted as a blue line the two models subtracted and divided by the error. It is clear from the figure that the overionized model fits the data much better, especially in the 0.7–1.0 and the 1.3–1.7 keV region. In the 0.5–1.7 keV range, the best-fitting single absorbed NEI model has a C-stat/d.o.f. = 334/72, a double absorbed NEI model has C-stat/d.o.f. = 119/64, and the overionized model with the parameters shown in table 1 has a C-stat/d.o.f. = 92/70. The overionized model therefore fits the data significantly better than any combination of a single or double absorbed underionized NEI or CIE model.

In the 0.7–1.0 keV energy range, the strongest emission feature is present at 0.87 keV which is not well-fitted by the non-overionized model. There are two main spectral emission options which could account for the emission feature at 0.87 keV: Fe XVIII emission, which has mainly emission lines at 0.77 and 0.87 keV, and the RRC
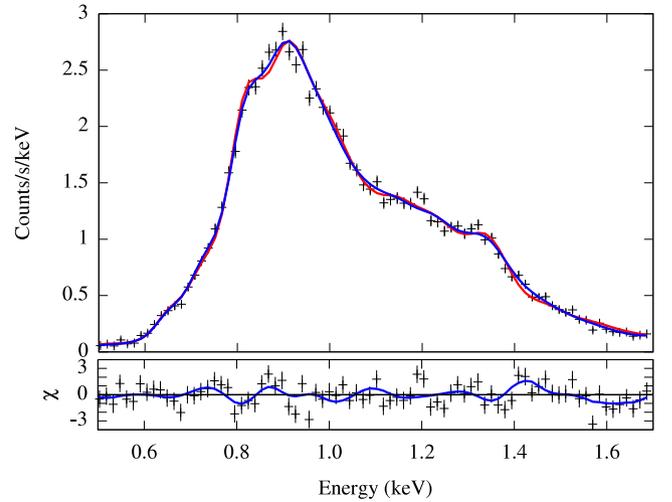


**Figure 5.** A close-up of the full spectrum, showing the effects of overionization in 3C 400.2. The red solid line shows the best-fitting model without using cooling, while the blue line shows the best-fitting cooling model for this region. The bottom panel shows the residuals of the non-cooling model with plotted in blue the difference between the cooling and non-cooling model divided by the error. This shows that the cooling model fits the spectral features around 0.87 and 1.4 keV much better than the non-cooling model.

of O VIII. Fe-L emission in general is often not well predicted by plasma models, as there are many different emission lines of which the strengths are not entirely known or understood (e.g. Bernitt et al. 2012). Of the different ionization states of Fe which produce Fe-L emission, the Fe-L lines produced by Fe XVII are often the most prominent in the hot plasmas found in SNRs, but they have a weak presence in 3C 400.2. Therefore, for a plasma to show strong Fe XVIII emission unaccompanied by Fe XVII emission, the ionization state of the Fe plasma needs to be high, with most of the Fe in Fe XVIII–XX ionization states. We have tried to fit this feature solely with a highly ionized Fe plasma, but due to other Fe emission lines this always resulted in an unacceptable fit, as the higher ionization states of Fe produce too much emission around 1.2 keV. The non-overionized NEI model attempts to fit the feature at 0.87 keV using a combination of the Ne IX Heα line and Fe XVIII emission. The Ne line has a centroid of 0.92 keV, however, which results in a bad fit. The overionized model fits this feature much better due to the addition of the O VIII RRC. In the 1.3–1.7 keV range, the non-overionized model shows large residuals, where it attempts to fit continuum emission using lines of Mg XI–XII, which has emission lines with centroids of 1.35 and 1.47 keV, respectively. The overionized model fits this region much better, using an Ne X RRC at 1.36 keV, which improves the fit with respect to the non-overionized model.

The above example shows that although the presence of overionization in 3C 400.2 is indeed subtle, the overionized models provide a significantly better fit to the data due to the presence of RRCs.

### 2.3 Spectra

In this section, we apply a cooling model to several regions of the remnant, which show significant differences in their plasma properties. In order to make sure that we did not miss equally good, but simpler models, we first attempted a single underionized NEI model, then a double underionized NEI model, then allowing the initial temperature of the lower *kT* NEI model to vary for every

spectrum shown, allowing in every case the abundances to vary only if the fit improved significantly. The $N_H$ was always allowed to vary. The C-stat/d.o.f. for the different fitting attempts are listed in Table 3.

### 2.3.1 Region 1: southern part of the remnant

This spectral extraction region coincides with the part of the remnant that is weak in X-ray emission, as is apparent from Fig. 4, but is the brightest in terms of optical emission (Winkler et al. 1993). This means that these parts of the remnant either show radiative shocks, where the shock velocity is lower than 200 km s$^{-1}$ for which the post-shock plasma cools efficiently, or the plasma has otherwise cooled to below $10^6$ K. This region has two models which fit nearly equally well. The first model (C-stat/d.o.f. = 81/87), of which the parameters are shown in Table 2, has similar properties to the model for the full region: it has an overionized ISM component and an underionized ejecta component with $kT_e = 3.1$ keV. Compared to the full model, however, the ejecta component contains no overabundance of Si. The feature in the spectrum around 1.8 keV is fitted by the Mg IX RRC of the cooling component. The $\tau = 3.20^{+0.89}_{-0.68} \times 10^{10}$ cm$^{-3}$ s combined with the high temperature produces a Si line with a centroid at ∼1.82 keV, which is too high to fit the feature. In addition, the Fe abundance is very poorly constrained: when left as a free parameter the best-fitting value raises to ∼250 times solar abundance, suggesting a plasma consisting purely of Fe. This is not realistic for 3C 400.2, especially when considering the best-fitting values for the other regions. Therefore, we fixed the Fe abundance at 15, close to the value obtained for the full region. The spectrum with the best-fitting model is shown in Fig. 6.

The second model for this region (C-stat/d.o.f. = 78.2/84) consists of two overionized (cooling) NEI components of which the parameters are listed in Table 3. The coolest component has $kT_e = 0.06$ keV, the lowest electron temperature of all regions in the remnant. The spectral features around 0.8–0.9 keV (see Fig. 7) are in this model fit by a combination of O VII–VIII RRCs at 0.74 and 0.87 keV. In addition, it shows an Ne IX RRC at 1.2 keV. The overall spectrum is dominated by emission from RRCs. The hotter component with $kT_e = 0.53$ keV shows the O VIII emission line coupled with an RRC, but otherwise again very little line emission. The abundances of both components are mostly solar, with only O
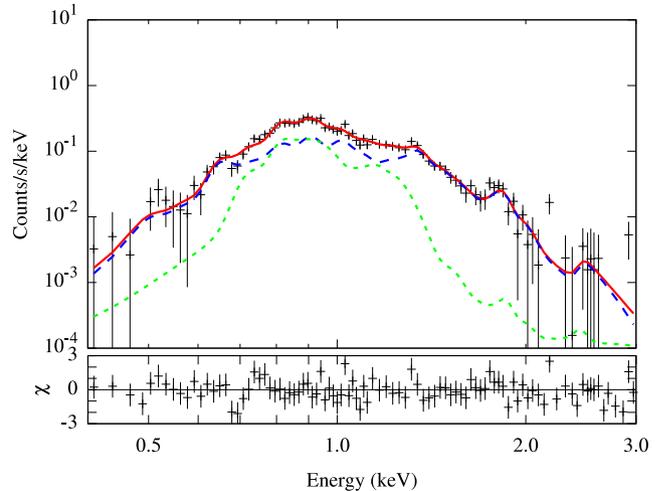


**Figure 6.** The spectrum of region 1, fitted with the model of which the parameters are listed in Table 2. The red solid line shows the complete model. The blue long dashed line shows the low-$kT$ NEI component while the green short-dashed line shows the high-$kT$ component.

being overabundant in the hotter component. Contrary to the full spectrum and spectra of other extraction regions, there is no supersolar abundance of Si, S or Fe present in the hot component for this region. The Fe abundance is sub-solar in the hotter component, while in the cooler component the temperatures are such that Fe has an ionization state <Fe XVII, which does not show significant emission in the X-ray band. The fact that there is practically no line emission from elements with higher mass than Mg is not unexpected in a plasma that is cooling rapidly, since the recombination and ionization rates of an element depend strongly on its charge.

The two models are statically almost equally probable. The first model (a combination of an under- and overionized NEI component) fits the 0.8–0.9 keV features slightly better, while the second model (with two overionized NEI components) fits the data better in the 0.4–0.8 keV region. Based on the abundances, especially the absence of Si and the high overabundance of Fe, we deem the double cooling NEI model slightly more realistic. The strong cooling fits well with the spatial coincidence with the optical emitting region in the remnant. But this model is different from the best-fitting models for the other regions.

### 2.3.2 Region 2: brightest part of the remnant

This region was extracted from the brightest part of the remnant in X-rays (see Fig. 4). The spectrum is shown in Fig. 7, top right. The best-fitting model again contains a hot ($kT_e = 3.59$ keV) underionized ($\tau = 1.87 \times 10^4$ cm$^{-3}$ s) NEI component with supersolar abundances, plotted as a green dashed line, and a cooler ($kT_e = 0.63$ keV) NEI component that is overionized, plotted as a blue dot–dashed line. As expected, the best-fitting model is very similar to the model of the full region, since the full spectrum is dominated by emission from the brightest part of the remnant. The plasma parameters of the hot component are identical to the full region within the errors, but the $N_H$ is significantly higher at $7.62^{+0.26}_{-0.24} \times 10^{21}$ cm$^{-2}$, compared to $6.08^{+0.15}_{-0.12} \times 10^{21}$ cm$^{-2}$. In addition, the initial temperature $kT_1 = 0.63$ keV for the cooler model is somewhat higher in this region than for the central region ($kT_1$=0.42), while the electron temperatures are identical within the errors. In general, the electron

**Table 2.** Parameters of the alternative model for region 1. The errors represent the 1$\sigma$ confidence interval.

| Component | Parameter | Unit | Value |
|---|---|---|---|
| Ejecta | $N_H$ | $10^{21}$ cm$^{-2}$ | $5.61^{+0.47}_{-0.45}$ |
| | $n_e n_H V$ | $10^{54}$ cm$^{-3}$ | $2.59^{+0.28}_{-0.26}$ |
| | $kT_e$ | | $3.20^{+0.89}_{-0.68}$ |
| | $\tau$ | $10^{10}$ cm$^{-3}$ s | $2.12^{+0.08}_{-0.08}$ |
| | Fe | | 015 (fixed) |
| | Luminosity | $10^{31}$ erg s$^{-1}$ | 4.2 |
| ISM | $n_e n_H V$ | $10^{56}$ cm$^{-3}$ | $7.49^{+2.13}_{-1.41}$ |
| | $kT_1$ | keV | $0.77^{+0.27}_{-0.15}$ |
| | $kT_e$ | keV | $0.19^{+0.01}_{0.01}$ |
| | $\tau$ | $10^{10}$ cm$^{-3}$ | $86.5^{+24.9}_{-21.8}$ |
| | Luminosity | $10^{31}$ erg s$^{-1}$ | 1.6 |
| | C-stat/d.o.f. | | 81/87 |

**Table 3.** Best-fitting model parameters for the spectral regions shown in Fig. 2. The abundances of the unlisted elements are fixed at their solar values. The errors represent a $1\sigma$ confidence interval. The C-stat/d.o.f. of the single NEI and double, non-cooling NEI models we attempted to fit to the data are listed.

| Parameter | Unit | Region | | | |
| --- | --- | --- | --- | --- | --- |
| | | 1 | 2 | 3 | 4 |
| $N_H$ | $10^{21}$ cm$^{-2}$ | $4.76^{+0.45}_{-0.88}$ | $7.62^{+0.26}_{-0.24}$ | $9.72^{+0.53}_{-1.32}$ | $5.49^{+0.23}_{-0.23}$ |
| $n_e n_H V$ | $10^{58}$ cm$^{-3}$ | $0.03^{+0.01}_{-0.01}$ | $1.79^{+0.42}_{-0.40}(\times 10^{-3})$ | $8.80^{+0.59}_{-2.70}(\times 10^{-3})$ | $0.275^{+0.42}_{-0.24}(\times 10^{-3})$ |
| $kT_1$ | keV | $0.53^{+0.04}_{-0.04}$ | – | – | – |
| $kT_e$ | keV | $0.25^{+0.04}_{-0.02}$ | $3.59^{+0.44}_{-0.39}$ | $0.71^{+0.06}_{-0.13}$ | $3.23^{+0.67}_{-0.72}$ |
| $\tau$ | $10^{10}$ cm$^{-3}$ s | $1.87^{+2.77}_{-1.87}$ | $2.03^{+0.06}_{-0.06}$ | $19.58^{+2.55}_{-1.08}$ | $1.94^{+0.17}_{-0.14}$ |
| O | | $2.67^{+0.91}_{-0.61}$ | – | – | – |
| Ne | | $<0.24$ | – | – | – |
| Si | | – | $2.75^{+0.81}_{-0.57}$ | $1.34^{+0.27}_{-0.18}$ | $9.53^{+25.05}_{-5.75}$ |
| S | | – | $5.05^{+1.62}_{-1.09}$ | $2.98^{+1.22}_{-0.56}$ | $12.2^{+60.8}_{-7.9}$ |
| Fe | | $0.62^{+0.20}_{-0.24}$ | $12.8^{+6.6}_{-2.8}$ | $0.47^{+0.28}_{-0.47}$ | $31.8^{+78.2}_{-4.5}$ |
| Luminosity | erg s$^{-1}$ | $2.7 \times 10^{31}$ | $4.1 \times 10^{32}$ | $9.53 \times 10^{31}$ | $1.4 \times 10^{32}$ |
| $n_e n_H V$ | $10^{58}$ cm$^{-3}$ | $0.16^{+0.15}_{-0.06}$ | $0.31^{+0.07}_{-0.06}$ | $2.08^{+0.13}_{-1.24}$ | $0.29^{+0.07}_{-0.05}$ |
| $kT_1$ | keV | $0.21^{+0.08}_{-0.02}$ | $0.63^{+0.11}_{-0.07}$ | $0.15^{+0.01}_{-0.01}$ | $0.32^{+0.03}_{-0.04}$ |
| $kT_e$ | keV | $0.06^{+0.01}_{-0.01}$ | $0.11^{+0.01}_{-0.01}$ | $0.10^{+0.01}_{-0.01}$ | $0.14^{+0.02}_{-0.01}$ |
| $\tau$ | cm$^{-3}$ s | $9.40^{+70.0}_{-9.40}(\times 10^{10})$ | $5.49^{+0.89}_{-0.87}(\times 10^{11})$ | $2.18^{+0.52}_{-2.18}(\times 10^{8})$ | $4.63^{+7.62}_{-4.63}(\times 10^{10})$ |
| O | | – | $3.08^{+0.53}_{-0.49}$ | – | – |
| Ne | | – | – | $2.07^{+0.25}_{-0.51}$ | $0.59^{+0.35}_{-0.15}$ |
| Luminosity | erg s$^{-1}$ | $5.3 \times 10^{26}$ | $1.6 \times 10^{31}$ | $7.2 \times 10^{28}$ | $7.5 \times 10^{30}$ |
| C-stat/d.o.f. | | 78.2/84 | 118.40/103 | 93.68/108 | 90.57/90 |
| C-stat/d.o.f. single NEI[a] | | 140.5/87 | 226/106 | 135/110 | 253/93 |
| C-stat/d.o.f. double NEI[b] | | 115/86 | 163/102 | 120/107 | 149/88 |

[a]The C-stat/d.o.f. of the fit attempted with a single NEI model.
[b]The C-stat/d.o.f. of the fit attempted with a double, non-cooling, NEI model.

temperatures for the cool component are very similar throughout the remnant, while the initial temperature shows significant variation.

### 2.3.3 Region 3: the northwestern part of the remnant

This region was taken from the utmost NW part of the *Chandra* FOV, which overlaps with the radio shell. The spectrum is shown in Fig. 7 bottom left. The hydrogen column of the best-fitting model of this region is $9.7 \times 10^{21}$ cm$^{-2}$. Although equal within the errors to the $N_H$ of region 2, it is significantly higher than the rest of the remnant. An increasing $N_H$ towards the NW of the remnant is consistent with the notion of the remnant expanding into a dense ISM cloud in the NW, where it is expected that the emission from the outer parts of the remnant travel through a larger amount of material than the emission from the inner parts. Significant variation in foreground absorption cannot be ruled out, however.

The best-fitting model again has a somewhat hotter, under-ionized NEI component with supersolar abundances combined with a cooler, overionized NEI component. However, the electron temperature of the hotter component is significantly smaller at $kT_e = 0.71$ keV, than those of the full spectrum and region 2 ($\approx 3.75$ keV), while the $\tau$ is significantly larger at $\sim 2 \times 10^{11}$ cm$^{-3}$ s, compared to $\tau = 2 \times 10^4$ cm$^{-3}$ s. And while the abundances are significantly super solar for Si and S, the Fe abundance is lower. It seems, therefore, that the Fe emission is confined to the central parts of the remnant.

### 2.3.4 Region 4: the centre of the remnant

Region 4 was taken from the SW part of the *Chandra* FOV, which is situated roughly in the centre of the total remnant, as can be deduced from the *ROSAT* image. The spectrum of this region has again similar parameters as the spectra from the full remnant and region 2. It is plotted in Fig. 7 bottom right, where the hot NEI component is plotted in a green dashed line, while the blue dot–dashed line represents the cooler NEI component. The $N_H = 5.49 \times 10^{21}$ cm$^{-2}$ of the best-fitting model for this region confirms the trend of increasing $N_H$ towards the NW part of the remnant. The plasma parameters of the hot component are equal within the errors to the temperatures of the full spectrum and the spectrum of region 2. Overall the model for this region confirms the notion of hot ejecta being confined to the central, brighter part of the remnant.

## 3 DISCUSSION AND CONCLUSION

From our spectral modelling, we obtain the following. The overall spectrum is well-fitted by a two-component NEI model plasma, of which one is *under*ionized with a high $0.71 < kT < 3.86$ keV and supersolar abundances of Si, S and Fe, while the other NEI component has a lower $0.06 < kT_e < 0.15$ keV, is *over*ionized and has approximately solar abundances. The central parts of the remnant show significantly higher abundances than the outer parts, which is apparent in region 3, where the abundances are significantly lower than in the centre. Region 1 coincides with the optically emitting region and shows two models which fit almost equally
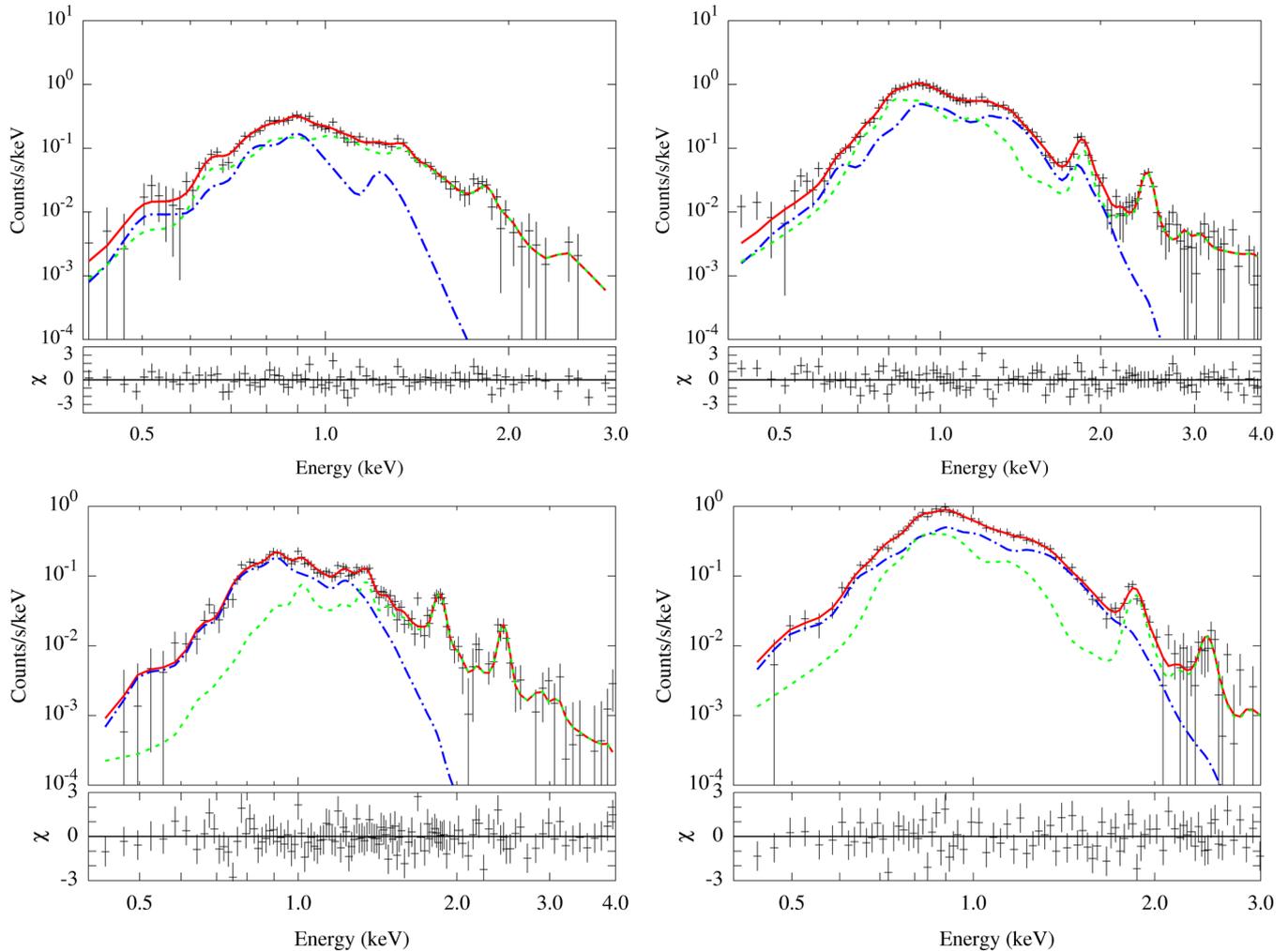
**Figure 7.** From left to right, top to bottom: spectra of region 1, region 2, region 3 and region 4. The models are described in the text. In general the green dashed line represents the cooler NEI component, while the dash–dotted blue line represent the hotter NEI component. The total model is plotted as a solid red line.

well. The first model shows similar properties to the central region, but with solar Si abundance, while the other model shows the lowest electron temperature of the whole remnant. Although different parts of the remnant show slightly different plasma properties in terms of initial temperature $kT_1$ and electron temperature $T_e$, the parameters are consistent with a hot ejecta plasma confined to the central part of the remnant, which is surrounded by a rapidly cooling, overionized swept-up ISM plasma.

### 3.1 Shocked mass

Using the parameters listed in Table 1, we can estimate of the amount of X-ray emitting mass, both in ejecta and ISM, present in the SNR. The emission measure of the cool component is $1.2 \pm 0.2 \times 10^{58}$ cm$^{-3}$. We use a distance of 2.5 kpc and a spherical volume of the emitting region. The spectral extraction region has a radius of 6.67 arcmin (4.85 pc), which corresponds to $V_{\text{total}} = 1.4 \times 10^{58} d_{2.5}^3$ cm$^3$. If we assume that the hot and the cool component are two separate plasmas, which both occupy part of the total emitting volume and which are in pressure equilibrium, we can get a unique solution for the density and shocked mass of the different components. The reason is that if $P_{\text{hot}} = P_{\text{cool}}$ then also $n_{\text{hot}} kT_{\text{hot}} = n_{\text{cool}} kT_{\text{cool}}$, where $n$ is the number density. For

$n_e = 1.2\ n_H$, the number density $n_H$ of a component is given by $(\text{EM}/1.2/V)^{1/2}$, so that

$$\left( \frac{\text{EM}_{\text{cool}}}{1.2 V_{\text{total}}(x)} \right)^{1/2} kT_{\text{cool}} = \left( \frac{\text{EM}_{\text{hot}}}{1.2 V_{\text{total}}(1-x)} \right)^{1/2} kT_{\text{hot}}, \quad (1)$$

where $\text{EM} = n_e n_H V$, $V_{\text{hot}} = (1-x)V_{\text{total}}$ and $V_{\text{cool}} = xV_{\text{total}}$. The above equation is equal for $x = 0.4$, so that $n_{\text{cool}} = 1.3(d_{2.5})^{-1/2}$ cm$^{-3}$ and $n_{\text{hot}} = 0.05(d_{2.5})^{-1/2}$ cm$^{-3}$. The respective masses are $M_{\text{cool}} = 8.7(d_{2.5})^{5/2}$ M$_\odot$ and $M_{\text{hot}} = 0.46(d_{2.5})^{5/2}$ M$_\odot$.

The total emitting volume is uncertain, since the line-of-sight depth of the remnant is unknown and therefore the emitting volume might be a factor of 2 greater. Note that the total mass in the remnant is larger than we calculate here, since the *Chandra* FOV covers about half of the total area of 3C 400.2, and we only estimate the mass of the plasma with $T > 10^6$ K.

The total mass of ejecta and ISM is quite similar to the mass found by Yoshita et al. (2001), who found a mass of $6.7 \pm 1.2$ M$_\odot d_{2.5}^{5/2}$ for the whole remnant. This is surprisingly small for a mature remnant like 3C 400.2, even if the remnant would be located at twice the assumed distance. However, it should be noted that this is only the X-ray emitting mass, and most of the mass may in fact be 'hiding' in the plasma cooled below $10^6$ K. The hot component, with supersolar abundances, only makes up a small fraction of the mass,

and the total ejecta mass seems very low if it is the ejecta component of a massive star. However, here it should be noted that only the inner regions of a massive star have enhanced metallicity. The total metallicity is a function of stellar mass, with stars around 13 M$_\odot$ producing only 0.3 M$_\odot$ of oxygen (Vink 2012). Therefore, a low mass of ejecta-rich material is consistent with a relatively low mass for the exploding massive star. This does, however, also suggest that the cooler plasma, which we designated ISM, may partially or completely consist of the hydrogen-rich envelope of the star. An explanation for why, in particular, ejecta material remains hot needs to be addressed by detailed hydrodynamical simulations, which should incorporate the effects of the stellar wind of the progenitor.

The low mass of the metal-rich component is also consistent with a Type Ia origin for the remnant. In that case, the cooler component could be solely shocked ISM. The enhanced iron abundances may indeed hint at a Type Ia origin, although the total mass of Fe at an abundance of 15 times solar is still much lower than the H mass. In addition, the association with the H I regions in the NW part of the remnant makes a core-collapse origin more likely. To settle on the origin of the remnant, it would be important to reconfirm the distance estimate of 2.5 kpc by Giacani et al. (1998), as a larger distance estimate would favour a core-collapse origin. It would also be helpful to identify a stellar remnant in 3C 400.2. The *Chandra* image does not show any evidence for a bright point source that could be the cooling neutron star.

## 3.2 Evolutionary scenario

The above densities suggest a hot, metal-enriched, tenuous plasma surrounded by a dense, cooler plasma which is cooling rapidly. This is consistent with the shell-like density structure expected from a Sedov evolutionary scenario. This is not the only MMR remnant in which such a temperature and density gradient is observed as Kawasaki et al. (2002) also find a two temperature best-fitting model and overionization in IC 443. They find that the central ejecta region has a temperature of 1 keV, compared to 0.2 keV in the outer layers. However, overionization is present only in the central ejecta rather than in the outer layers, while we find overionization in the outer layers and not in the ejecta.

In the Introduction, we mentioned three different evolutionary scenarios that might explain the centrally peaked X-ray emission: the evaporating cloudlet scenario (White & Long 1991), the Cox et al. (1999) scenario with high surrounding density including thermal conduction, and the relic X-ray emission scenario. Our observations show that the plasma is best explained by a low-density, hot interior surrounded by a high-density, lower temperature plasma. The total X-ray emitting mass is relatively low, for a mature remnant. But this is likely an indication that most of the remnant mass is not emitting in X-rays. In addition, overionization is only present in the cool plasma, suggesting that it is cooling more efficiently than the hot plasma. Our results are perhaps most naturally explained by the simplest evolutionary scenario of the three: the relic X-ray emission scenario (Rho & Petre 1998). As a result of the high ambient medium density, the outer layers have cooled below temperatures capable of emitting in X-rays relatively early in the evolution of the SNR. The interior is still hot and has a low density and is therefore not cooling efficiently, but the density is still high enough for substantial X-ray emission from the interior. Thermal conduction may be occurring, but we do not find evidence for overionization as a result of rapid cooling for the hot centrally confined plasma. Moreover, the X-ray emitting plasma inside the remnant is clearly not isothermal, as indicated by the model of Cox et al. (1999).

As a final note, thermal conduction has mainly been introduced to models explaining the evolutionary scenarios of MMRs based on the then current observations of generally lower spectral and spatial resolution, which showed little to no temperature gradient in the remnants. However, more modelling is needed to understand whether local density alone determines if a remnant will evolve into an MMR, or whether some other conditions, such as pre-supernova evolution or ejecta structure, are important as well.

The overionization of thermal plasmas can quite naturally occur in MMRs. The high initial ISM density allows the plasma to reach CIE on a time-scale smaller than the age of the remnant, after which a combination of adiabatic and radiative cooling can make the cooling rate of the plasma higher than the recombination rate, as shown in Broersen et al. (2011). The higher surrounding ISM density of MMRs might then be the determining factor for the occurrence of overionization compared to non-MMRs, as already noted in Vink (2012). Indeed, all remnants cool adiabatically and by radiation, but not all remnants expand in a high enough ISM density to reach CIE and then overshoot to overionization.

## 4 SUMMARY

We have analysed an archival *Chandra* observation of the mixed morphology remnant 3C 400.2. Our results can be summarized as follows.

(i) The plasma of the mixed-morphology SNR 3C 400.2 is best fitted by a combination of a hot, underionized plasma with low density, and a cooler, overionized plasma with high density. To our knowledge, this is the first evidence for a combination of an overionized outer shell surrounding an ejecta-rich, underionized inner region in an MMR.

(ii) The hot plasma shows significant overabundances of Fe, Si and S, suggesting an ejecta origin, with Fe enhanced in the central part.

(iii) Overionization is significantly present in all parts of the remnant covered by the *Chandra* FOV.

(iv) The X-ray emitting masses of the plasma components are $M_{\rm cool} = 8.7(d_{2.5})^{5/2}$ M$_\odot$ and $M_{\rm hot} = 0.46(d_{2.5})^{5/2}$ M$_\odot$.

(v) This low overall mass suggests that most of the X-ray emitting mass is from a mix of metal-rich and hydrogen-rich (envelope) ejecta from a not too massive core-collapse supernova, or the remnant has a Type Ia origin.

(vi) The observations are best explained by a scenario in which the centrally peaked X-ray emission is caused by a hot, metal-enriched, tenuous plasma. Due to the high surrounding ISM density the outer parts of the remnant have cooled efficiently towards a temperature below which they do not radiate in observable X-ray emission.

(vii) The presence of overionization in the outer parts of the remnant can be naturally explained by efficient cooling due to a high ISM density in combination with adiabatic expansion.

## REFERENCES

Ambrocio-Cruz P., Rosado M., de La Fuente E., 2006, Rev. Mex. Astron. Astrofis., 42, 241

Anders E., Grevesse N., 1989, Geochim. Cosmochim. Acta, 53, 197

Arnaud K. A., 1996, in Jacoby G. H., Barnes J., eds, ASP Conf. Ser. Vol. 101, Astronomical Data Analysis Software and Systems V. Astron. Soc. Pac., San Francisco, p. 17

Bernitt S. et al., 2012, Nature, 492, 225

Broersen S., Vink J., Kaastra J., Raymond J., 2011, A&A, 535, A11

Cash W., 1979, ApJ, 228, 939

Condon J. J., Cotton W. D., Greisen E. W., Yin Q. F., Perley R. A., Taylor G. B., Broderick J. J., 1998, AJ, 115, 1693

Cox D. P., Shelton R. L., Maciejewski W., Smith R. K., Plewa T., Pawl A., Różyczka M., 1999, ApJ, 524, 179

Dubner G. M., Giacani E. B., Goss W. M., Winkler P. F., 1994, AJ, 108, 207

Giacani E. B., Dubner G., Cappa C., Testori J., 1998, A&AS, 133, 61

Giuliani A., Tavani M., Bulgarelli A., Striani E., Sabatini 2010, A&A, 516, L11

Harrus I. M., Hughes J. P., Singh K. P., Koyama K., Asaoka I., 1997, ApJ, 488, 781

Kaastra J. S., Mewe R., Nieuwenhuijzen H., 1996, in Yamashita K., Watanabe T., eds, UV and X-ray Spectroscopy of Astrophysical and Laboratory Plasmas. Universal Academy Press, Uppsala, p. 411

Kawasaki M. T., Ozaki M., Nagase F., Masai K., Ishida M., Petre R., 2002, ApJ, 572, 897

Kawasaki M., Ozaki M., Nagase F., Inoue H., Petre R., 2005, ApJ, 631, 935

Lazendic J. S., Slane P. O., 2006, ApJ, 647, 350

Long K. S., Blair W. P., Matsui Y., White R. L., 1991, ApJ, 373, 567

Lopez L. A., Pearson S., Ramirez-Ruiz E., Castro D., Yamaguchi H., Slane P. O., Smith R. K., 2013, ApJ, 777, 145

Masai K., 1997, A&A, 324, 410

Miceli M., Bocchino F., Decourchelle A., Ballet J., Reale F., 2010, A&A, 514, L2

Milne D. K., 1979, Aust. J. Phys., 32, 83

Ohnishi T., Koyama K., Tsuru T. G., Masai K., Yamaguchi H., Ozawa M., 2011, PASJ, 63, 527

Rho J., Petre R., 1998, ApJ, 503, L167

Rosado M., 1983, Rev. Mex. Astron. Astrofis., 8, 59

Saken J. M., Long K. S., Blair W. P., Winkler P. F., 1995, ApJ, 443, 231

Schneiter E. M., de La Fuente E., Velázquez P. F., 2006, MNRAS, 371, 369

Shelton R. L., Cox D. P., Maciejewski W., Smith R. K., Plewa T., Pawl A., Różyczka M., 1999, ApJ, 524, 192

Smith R. K., Hughes J. P., 2010, ApJ, 718, 583

Spitzer L., Jr, 1981, Physical Processes in the Interstellar Medium. Wiley, New York

Tao L., 1995, MNRAS, 275, 965

Uchida H. et al., 2012, PASJ, 64, 141

Uchiyama Y., Funk S., Katagiri H., Katsuta J., Lemoine-Goumard M., Tajima H., Tanaka T., Torres D. F., 2012, ApJ, 749, L35

Vink J., 2012, A&AR, 20, 49

White R. L., Long K. S., 1991, ApJ, 373, 543

Winkler P. F., Olinger T. M., Westerbeke S. A., 1993, ApJ, 405, 608

Yoshita K., Tsunemi H., Miyata E., Mori K., 2001, PASJ, 53, 93

This paper has been typeset from a TEX/LATEX file prepared by the author.